

Modelling, Simulating and Visualizing the Cahn-Hilliard-Cook Field Equation

K.A. Hawick and D.P. Playne

Computer Science, Institute of Information and Mathematical Sciences,
Massey University, North Shore 102-904, Auckland, New Zealand

{k.a.hawick,d.p.playne}@massey.ac.nz, Tel: +64 9 414 0800 Fax: +64 9 441 8181

Abstract

The Cahn-Hilliard-Cook equation continues to be a useful model describing binary phase separation in systems such as alloys and other physical and chemical applications. We describe our investigation of this field equation and report on the various discretisation schemes we used to integrate the system in one-, two- and three-dimensions. We also discuss how the equation can be visualised effectively in these different dimensions and consider how these techniques can usefully be applied to other partial differential equations.

Keywords: alloy; pde; 3-D visualisation; interactive; phase separation.

1 Introduction

This paper describes an investigation of phase separation in a binary system. The Cahn-Hilliard-Cook (CHC) *equation* gives a reasonable representation of phase separation and decomposition in a binary system, providing one accepts that it cannot be applied successfully without resorting to numerical methods. The Cahn-Hilliard-Cook *theory* is essentially a mean field approximation to the time-dependent Ginzburg-Landau equation for the free energy of a binary system. The differential equation that describes the phase separation cannot be solved analytically, and requires further approximation. Alternatively it can be solved numerically for a particular set of parameters.

This paper extends work begun in 1988 and included in [Hawick, 1991]. Recent work on faster general purpose computers has enabled greater exploration of the CHC parameter space and interactive visualisation of two- and three-dimensional systems.

2 Cahn-Hilliard-Cook Equation

We consider a system of a mixture of two atomic species A and B, with some variable c_i that expresses which species is at a particular site i . Cahn-Hilliard-Cook (CHC) theory replaces these rapidly varying atomic concentration variables $\{c_i\}$ by a more smoothly varying continuous field variable $\phi(\mathbf{r})$ which represents an average value of the excess concentration of A-atoms over a macroscopic spatial cell. The field variable is a scalar defined to lie on $[-1, 1]$, with the extremum values representing an excess of B-atoms (-1) or an excess of A-atoms ($+1$).

2.1 Helmholtz Free Energy of a Binary Solution

Consider the Helmholtz free energy for an isotropic binary solid in solution and having a non-uniform composition. A convenient form for this is the Ginzburg-Landau functional [Cahn and Hilliard, 1959]:

$$\frac{\mathcal{F}\{\phi(\mathbf{r})\}}{k_b T} = \int_V \left\{ f\{\phi(\mathbf{r})\} - \frac{H}{k_b T} \phi(\mathbf{r}) + \frac{1}{2d} [R \nabla \phi(\mathbf{r})]^2 \right\} d\mathbf{r} \quad (1)$$

The scalar field $\phi(\mathbf{r})$ describes the composition as a function of position \mathbf{r} . The interaction range is described by $\frac{R}{d}$ and the applied field is H . For this work, the atomic concentration is fixed, so that the applied field H is set identically to zero for an equal concentration of A-type and B-type atoms.

The phase separating alloy may be thought of as a set of macroscopic cells, each containing a volume of space and a number of atomic sites. These cells must be large enough for a local instantaneous free energy function $f(\mathbf{r})$ to be defined, but small enough that the effect of ‘relevant’ short length scale composition fluctuations are not integrated out. It is convenient to write this local free energy density function $f\{\phi(\mathbf{r}, t)\}$ in the Landau form:

$$f\{\phi(\mathbf{r}, t)\} = f_0 - \frac{1}{2}b(\phi(\mathbf{r}, t))^2 + \frac{1}{4}u(\phi(\mathbf{r}, t))^4 + \dots \quad (2)$$

where $b, u > 0$.

The form of the local free energy for one cell has a double minimum for the homogeneous case and relaxes towards a single minimum after the quench. A distinction is usually drawn between different regions of the phase diagram from points on this double well functional. The central local maximum in the free energy is separated from the two minima by points of inflection where $f'' \equiv \frac{d^2 f}{d\phi^2} = 0$. These points mark the division between the metastable $f'' > 0$ and unstable $f'' < 0$ regimes. The locus of points where $f'' = 0$ defines the spinodal curve in the temperature-composition phase diagram.

For a quench in a system of given composition c_0 between the spinodal points, f'' is negative and the curve is always convex-down causing a negative \mathcal{F} . In this case there is no barrier to a fluctuation of any amplitude and the kinetic process is governed solely by diffusion. For a c_0 lying outside the spinodal points only large amplitude composition fluctuations will lower the free energy of the system. This requires sufficient thermal energy in the system to overcome the barrier.

2.2 Conservation Law

In a real material the number of atoms of a given species is conserved and hence the concentration field must also be. This is expressed by:

$$\frac{1}{V} \int_V \phi(\mathbf{r}, t) d\mathbf{r} = c_A \quad (3)$$

where V is the system volume, and c_A the concentration of atomic species A . This conservation law implies that the local concentration field obeys a continuity equation of the form:

$$\frac{d\phi(\mathbf{r}, t)}{dt} + \nabla \cdot \mathbf{j}(\mathbf{r}, t) = 0 \quad (4)$$

This defines a concentration current $\mathbf{j}(\mathbf{r}, t)$, assumed to be proportional to the gradient of the *local* chemical potential difference¹ $\mu(\mathbf{r}, t)$ with constant of proportionality m , the mobility.

$$\mathbf{j}(\mathbf{r}, t) = -m\nabla\mu(\mathbf{r}, t) \quad (5)$$

The chemical potential difference is, by definition:

$$\mu(\mathbf{r}, t) = \frac{d\mathcal{F}\{\phi(\mathbf{r}, t)\}}{d\phi(\mathbf{r}, t)} \quad (6)$$

¹The global chemical potential is identified with the field term in the Ising Hamiltonian and is identically zero for a system of conserved concentration

Where \mathcal{F} is the Landau functional given above in equation 1. Differentiating this functional with respect to ϕ and assuming a scalar mobility yields the chemical potential difference as:

$$\mu(\mathbf{r}, t) = \left. \frac{\partial f}{\partial \phi} \right|_T - \frac{R^2}{d} k_b T \nabla^2 \phi(\mathbf{r}, t) \quad (7)$$

which when substituted into the continuity equation 4 gives the Cahn-Hilliard equation [Cahn and Hilliard, 1959] for the concentration field.

$$\frac{\partial \phi(\mathbf{r}, t)}{\partial t} = m \nabla^2 \left(\left. \frac{\partial f(\phi(\mathbf{r}, t))}{\partial \phi} \right|_T - K \nabla^2 \phi(\mathbf{r}, t) \right) \quad (8)$$

Where the parameter K is defined as:

$$K = \frac{R^2}{d} k_b T \quad (9)$$

Expanding equation 8 we obtain:

$$\frac{\partial \phi}{\partial t} = m \nabla^2 (-b\phi + u\phi^3 - K \nabla^2 \phi) \quad (10)$$

It is usual to truncate the series in the free energy at the ϕ^4 term, although some work has used up to the ϕ^6 term [Tuszynski et al., 1990].

2.3 Cahn-Hilliard Theory

Equation 8 is non-linear and therefore cannot be solved analytically, although a numerical approach is possible. As described in [Cahn and Hilliard, 1959], the Cahn-Hilliard theory proceeds by linearising the equation around $\phi = c_A$ to obtain:

$$\frac{\partial(\phi - c_A)}{\partial t} = m \nabla^2 \left(\left. \frac{\partial f}{\partial \phi} \right|_{T, c_A} - K \nabla^2 (\phi - c_A) \right) \quad (11)$$

This is Fourier-transformed using:

$$\Phi(\mathbf{q}, t) = \int e^{i\mathbf{q} \cdot \mathbf{r}} (\phi(\mathbf{r}, t) - c_A) d\mathbf{r} \quad (12)$$

to yield:

$$\Phi(\mathbf{q}, t) = \Phi(\mathbf{q}, t=0) e^{B(\mathbf{q})t} \quad (13)$$

and the time amplification factor B is given by:

$$B(\mathbf{q}) = -m\mathbf{q}^2 \left(\left. \frac{\partial f}{\partial \phi} \right|_{T, c_A} + K\mathbf{q}^2 \right) \quad (14)$$

The structure function can be then obtained as an auto-correlation of the concentration field:

$$S(\mathbf{q}, t) = \langle \Phi(-\mathbf{q}, t) \Phi(\mathbf{q}, t) \rangle|_T \quad (15)$$

Re-writing this in terms of the values just prior to the quench gives:

$$S(\mathbf{q}, t) = \langle \Phi(-\mathbf{q}, t=0) \Phi(\mathbf{q}, t=0) \rangle|_T e^{2B(\mathbf{q})t} \quad (16)$$

The prefactor in 16 is the static structure factor of the initial state at T_0 , just prior to the quench.

$$S_0(\mathbf{q}) = \langle \Phi(-\mathbf{q}, t=0) \Phi(\mathbf{q}, t=0) \rangle|_{T=T_0} \quad (17)$$

It is evident then that the linearised Cahn-Hilliard theory implies that fluctuations of \mathbf{q} present in the initial state will grow exponentially with time following the quench if $B(\mathbf{q}) > 0$ but will decay to zero for $B(\mathbf{q}) < 0$. There is an implied critical wavevector \mathbf{q}_c for which $B(\mathbf{q}) \equiv 0$. There has been some controversy in the literature [Binder, 1989] about the validity of this linearised theory, but it seems clear that the theory is not valid for systems with short range interactions such as the alloy model used in this work. A full discussion of the failings of the theory is left to [Binder, 1989].

2.4 Cook's Extension to Cahn-Hilliard

The Cahn-Hilliard theory as described above is essentially a mean field theory. It approximates the interactions between the concentration variables by a mean value and ignores thermal fluctuations. It might be expected that consequently it will incorrectly predict the dynamic behaviour of the system. A simple extension to equation 8 was considered by Cook [Cook, 1970] in which an additional random force term ζ is added to give:

$$\frac{\partial \phi(\mathbf{r}, t)}{\partial t} = m \nabla^2 \left(\frac{\partial f(\phi(\mathbf{r}, t))}{\partial \phi} \Big|_T - K \nabla^2 \phi(\mathbf{r}, t) \right) + \zeta(\mathbf{r}, t) \quad (18)$$

This noise term is assumed to come from the very short time scale phonon modes of the alloy and is required to have the following properties:

$$\langle \zeta(\mathbf{r}, t) \rangle = 0 \quad (19)$$

$$\langle \zeta(\mathbf{r}, t) \zeta(\mathbf{r}', t') \rangle = -2k_b T m \nabla^2 \delta(\mathbf{r} - \mathbf{r}') \delta(t - t') \quad (20)$$

Equations 19 and 20 express two things. There is no overall drift force and the noise is uncorrelated in time, but partially correlated in space such that there are no long wavelength components in the noise spectrum. The magnitude of the noise is set by $k_b T$ and mobility m . More specifically, the ∇^2 in equation 20 expresses the conservation law for the field. A random force component which 'piles up' matter at one site must be exactly balanced by force contributions at neighbouring sites which deplete those sites of matter. The form of equation 20 ensures this is so.

The Cook noise term does not rescue the linearised theory from invalidity, but it does have important implications for numerical work. To date there have been no attempts to numerically solve equation 18, and is it still controversial whether the Cook noise term plays an important role in the long time dynamics of the alloy [Toral et al., 1988].

3 Numerical Solutions

Although equations 8 and 18 are highly non-linear in nature, it is nevertheless possible to numerically integrate them in time to follow the structure evolution. Two numerical methods suggest themselves for equations of this type, namely the well known finite differencing method and a lesser known spectral method such as the Fourier analysis and cyclic reduction algorithm (FACR) [Buzbee et al., 1970]. The former is relatively easy to set up and has been considered by other authors for very simple cases [Toral et al., 1988, Milchev et al., 1988]. Unfortunately it is fairly demanding of computational power to perform the time and spatial integrals of realistic systems. The FACR algorithm is more complicated to implement and while in general a spectral method is more suited to a studying a theory formulated in terms of waves in Fourier space, this algorithm is not suitable for comparison with the Monte Carlo simulations in position space since it does not yield a real space representation of the concentration field.

3.1 Finite Differencing Schemes

Consider equation 18 that we wish to integrate numerically. This can be re-cast as:

$$\frac{\partial \phi(\mathbf{r}, t)}{\partial t} = P(\mathbf{r}) \quad (21)$$

All the spatial dependence is now contained in the functional P , which can be discretised using a centred space representation. The scheme is illustrated below, initially only for a one dimensional system.

$$\begin{aligned} P_j^{(n)} = & \frac{M}{\Delta x^2} (-b\phi_{j-1}^{(n)} + 2b\phi_j^{(n)} - b\phi_{j+1}^{(n)} \\ & + u\phi_{j-1}^{(n)3} - 2u\phi_j^{(n)3} + u\phi_{j+1}^{(n)3} \\ & + \frac{1}{\Delta x^2} [-K\phi_{j-2}^{(n)} + 4K\phi_{j-1}^{(n)} - 6K\phi_j^{(n)} \\ & + 4K\phi_{j+1}^{(n)} - K\phi_{j+2}^{(n)}] \\ & + \zeta_j^{(n)} \end{aligned} \quad (22)$$

where the spatial mesh of N points is indexed by $1 < j < N$, and the time discretisation mesh is indicated by $0 < n < \infty$. This centred space finite difference scheme is second order accurate in the spatial mesh size Δx and is optimal for a

diffusion equation like the Cahn-Hilliard equation. Higher order accuracy in space is likely to be inherently unstable, and lower order is too limiting in terms of numerical accuracy [Press et al., 1988]. This scheme was indeed found to be the best and can readily be extended to two- and three-dimensions.

It now remains to choose a discretisation scheme for the time domain. This is considerably more difficult. The obvious choice is the Forward-Time or Euler scheme and is only first order accurate in time. It is easily implemented as:

$$\phi_j^{(n+1)} = \phi_j^{(n)} + P_j^{(n)} \cdot \Delta t \quad (23)$$

In this scheme, each new grid point value of ϕ depends only on the previous generation of values. This method requires a small time-step but was only found to be sufficiently stable for the one dimensional system. A better scheme is required for higher dimensions. There are a number of widely used reliable schemes available [Press et al., 1988], but the computational demands of such schemes prohibit their use, particularly in the present case where the computer technology is already being stretched to its limits in terms of speed.

The problem with the forward differencing scheme described above can be identified with the non-symmetric way it uses available data to perform each time step. Three methods considered here for evaluating the ∇^2 operator in the Cahn-Hilliard equation. The $\nabla^2 \cdot \nabla^2 = \nabla^4$ contributes no new problem, it merely compounds the old one.

The staggered-leapfrog scheme is a well known method that is second order in time. It requires information from the two previous time steps to compute the next value and can be written as:

$$\phi_j^{(n+1)} = \phi_j^{(n-1)} + P_j^n \cdot \Delta t \quad (24)$$

This additional storage requirement is a disadvantage over the simpler forward differencing scheme, particularly for the large grids required. The staggered-leapfrog is surprisingly no improvement and indeed is considerably less stable for certain values of K , u , b and M . This anomaly can be understood by considering the effect of the alternating mesh used by this scheme. The two alternating meshes are in fact decoupled, so that drift instabilities can arise between the two meshes. This leads to rapid divergence of the field in opposing directions for each mesh.

This decoupling problem can be partially alleviated using the Lax scheme, whereby grid points used in the time-step calculation are replaced by interpolated values at half grid points $\phi_{j+\frac{1}{2}}^n$. This method uses a small *numerical viscosity* term obtained by adding a small fraction f of the value on the alternate grid to the grid calculation. This is somewhat unphysical and furthermore tends to damp out high frequency components in the evolving field. For this reason a better scheme is the two-step Lax-Wendroff method. In this scheme, the first operation is to evaluate the interpolated half-step points in

time *and* space according to the Lax scheme, and then to use these intermediate values (which are discarded afterwards) to make a single time step movement.

$$\begin{aligned} \phi_{j+\frac{1}{2}}^{(n+\frac{1}{2})} &= \frac{1}{2} (\phi_{j+1}^{(n)} + \phi_j^{(n)}) + \frac{\Delta t}{2 \times 2} (P_{j+1}^{(n)} + P_j^{(n)}) \\ \phi_j^{(n+1)} &= \phi_j^{(n)} + \frac{\Delta t}{2} (P_{j-\frac{1}{2}}^{(n+\frac{1}{2})} + P_{j+\frac{1}{2}}^{(n+\frac{1}{2})}) \end{aligned} \quad (25)$$

This is a good *explicit* scheme found. It allows quite large time steps, and therefore relatively fast computation times for a given evolution time and very low mesh drifting despite low numerical viscosity.

The well known Runge-Kutta numerical integration method is more cumbersome to implement but we have experimented with both second order (also known as the midpoint method) and the fourth order scheme. Both perform well and on 21st century computer systems where we can afford the extra working storage

The schemes are summarised in table 1, they are described in [Allen and Tildesley, 1987, Press et al., 1988].

The upper limits on stability are determined from the highest value of Δt that will converge for all reasonable parameter values *and* gives the *same* results with a 10% variation in Δt . The lower limit of stability is quoted as 0.00001, this resulting from the 32-bit real number precision employed in the calculations. This can be reduced at the expense of computational time, by resorting to 64-bit arithmetic.

3.2 Meaning of the CHC Parameters

The Cahn-Hilliard-Cook equation is derived with parameters that are not obviously related to experimentally measurable properties of an alloy. The parameters u , b , m , and K that appear in equation 10 *can* be related to the microscopic parameters in the lattice gas model, by a comparison with mean field theory.

The mobility m appears only as a multiplicative constant and effectively controls the time scale. In numerical work it can be absorbed into the time-step of integration. The parameter $K = \frac{R^2}{d} k_b T$ reduces to $K = \frac{k_b T}{d}$ for the nearest neighbour interaction model, since:

$$R^2 = \frac{\sum_{i,j} (r_i - r_j)^2 (V_{i,j}^{A-A} + V_{i,j}^{B-B} - 2V_{i,j}^{A-B})}{\sum_{i,j} (V_{i,j}^{A-A} + V_{i,j}^{B-B} - 2V_{i,j}^{A-B})} \quad (26)$$

where the $V_{i,j}^{c_i-c_j}$ are the Ising coupling parameters and d is the spatial dimension.

This means K , like u and b have units of free energy density, and all contain a factor of $k_b T$ which can also be absorbed into the mobility or time scale. Standard mean field theory

<i>Scheme</i>	<i>Range of Stability in Δt</i>	<i>Storage Requirement</i>	<i>Efficiency</i>	<i>Comment</i>
FTCS (Euler)	0.01 – 0.00001	Low	Poor	Physical but inaccurate
Staggered-leapfrog	0.001 – 0.00001	Medium	Medium	Unreliable
Lax	0.05 – 0.00001	Medium	Good	Unphysical viscosity
Lax-Wendroff	0.1 – 0.00001	High	Very Good	Physical and reliable
Runge-Kutta 4	0.2 – 0.00001	Medium	Very Good	Physical and very reliable

Table 1: Finite Difference Schemes as applied to the Cahn-Hilliard-Cook Equation. Note that computational efficiency also takes account of how high the time step may be, since it is possible to integrate to longer simulated times much faster with an algorithm which allows large time steps.

for the Ising model [Binder, 1988] shows that the parameter b controls the quench temperature for the model through the relation $b = \frac{T}{T_c^{MF}} - 1$, where T_c^{MF} is the mean field critical temperature discussed in chapter 2. This leaves the parameter u undetermined, but for numerical work it is convenient to set it to unity and employ the ratio $\frac{b}{u}$ to determine the interaction strength J^{A-A} . The combination of parameters $b = u = M = K = 1$, then corresponds to an infinite quench for an unknown linear time scale.

Increasing K corresponds to increasing the range of the model interactions, while changing the sign of K changes the ground state of the model to that of an ordered system, the exact nature of which will depend on the global concentration of A-atoms [Tuszynski et al., 1990]. This present work considers only positive values of K .

Specific values of the Cook noise term appear less important than the fact of its mere presence. The correct magnitude is set by equation 20 and a convenient form is that of a Gaussian distribution centred on zero with $\sigma^2 = 2k_b T m$ in the units of the simulation, and with the properties dictated by equations 19 and 20.

4 One-Dimensional System

A natural place to begin investigations is a symmetric quench from a temperature T_0 well above the two-phase coexistence curve to one below it T_1 . A completely random starting configuration is a good approximation to the case $T_0 \rightarrow \infty$.

A simple illustration of the important properties of the Cahn-Hilliard-Cook equation can be drawn from experiments with a one dimensional simulation. A one dimensional system of 4096 sites was initialised randomly with $\phi_j \in [-0.25, 0.25]$, $\sum_j \phi_j = 0$, and numerically integrated with the parameter values $K = m = b = u = 1$ using a spatial mesh of $\Delta x = 1$

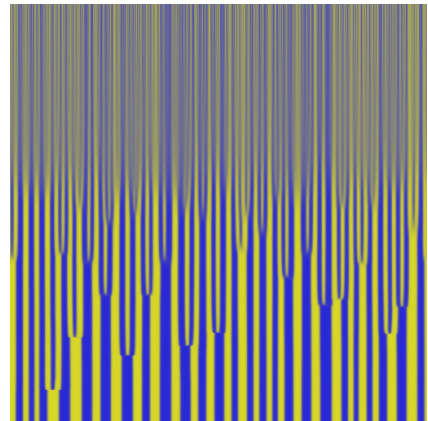


Figure 1: 1-D CHC system with space horizontally, and time downwards, plotted in \log_2 time, with each time row at times 0, 1, 2, 4, 8, 16, ...

and a time step of $\Delta t = 0.01$ with the Forward-Time Centred Space (FTCS) scheme. The initially homogeneous mix separates out into two well defined phases. The real space evolution can be represented as an intensity plot for the composition field ϕ as a function of time vertically and space horizontally. The initial grey mix separated into a spatially modulated two phase structure. This can also be tracked for a longer time by examining the composition population.

It appears that for a pseudo-infinite quench, growth occurs, but slowly. The Cook noise term is zero for a quench to zero temperatures. At a temperature of $\frac{T_c}{4}$, the Cook noise term accelerates the initial growth process substantially. At a higher still temperature of $\frac{T_c}{2}$, there is sufficient thermal energy in the model system that the Cook term appears to have a less dramatic effect, although it still accelerates growth.

Figure 1 shows the formation of like domains of cells and the merging of domains over time. Time is plotted on a \log_2

scale to emphasise all timescales of the process. The resulting tree diagram shows how domains merge and as discussed in section 7 the number of separate domains N_D can be approximated by a power law in time t .

5 Two-Dimensional System

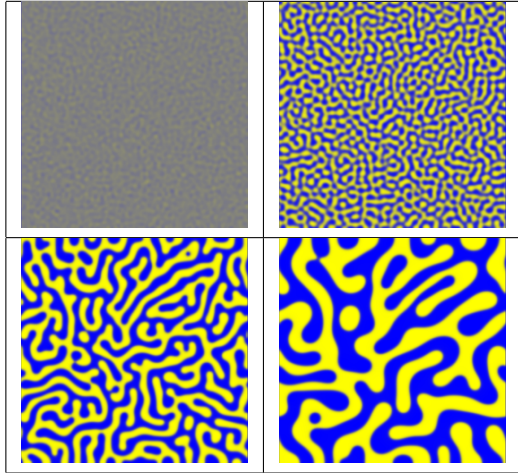


Figure 2: 2-Dimensional CHC simulation with 256×256 cells at $t = 256$ (top left), $t = 2048$ (top right), $t = 16384$ (lower left) and $t = 131072$ (lower right)

In two-dimensions the cells are able to interact in a different way from the simple left/right nearest neighbour interactions in a 1-D system. Figure 2 shows the time evolution of the composition population in a two-dimensional system. The random initial configuration forms domains which then coarsen and grow to form striated interleaving structures. Surface tension gradually draws these into just two separated domains, providing there is sufficient thermal energy in the system.

6 Three-Dimensional System

It is more difficult to track a three-dimensional system visually and more reliance must be placed on the size characterisation of the separating phases by averaged Fourier transforms. The peaks vary considerably in magnitude, but the peak positions can be well determined, and mapped to characteristic sizes.

The technology of visualisation in one- and two-dimensions has been well developed, however visualising the three-dimensional simulation is significantly more challenging. In this research the JOGL API [Bryson and Russell, 2007] to the OpenGL library is used to render the three-dimensional simulation as a cube of cells. Each cell is rendered as a sphere

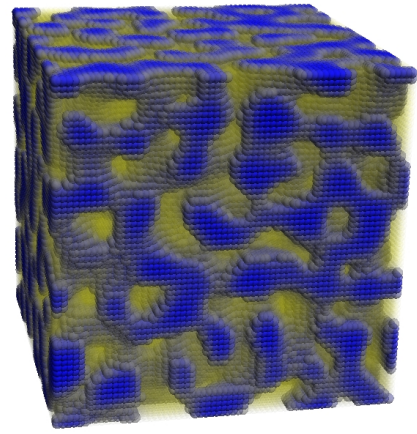


Figure 3: 3-Dimensional CHC configuration with $64 \times 64 \times 64$ cells.

and coloured relative to its atomic concentration value. The colour and opacity of each sphere $C_{x,y,z}$ is calculated according to the cell value $\sigma_{x,y,z}$ defined by equation 27.

A mixture of transparency combinations was explored and the combination of having one domain as mostly transparent and the other relatively opaque allows the domain growth inside the cube to be seen the most clearly. One domain is seen as a complicated 3-D shape and the other as a cloud surrounding the shape. Navigating around the cube in 3-D allows the domains to be seen for the entire simulation.

7 Domain Growth

A number of macroscopic properties of the CHC system can be measured to characterise system bulk behaviour. Domains can be counted using a graph labelling technique and averaging over multiple sample random starting conditions and different temporal trajectories we can obtain a meaningful fit to the number of domains $N_D(t)$ as it varies with time. Figure 4 shows the number of distinct domains in different dimensional systems plotted against time. As can be seen from the log-log plots the system is quite well approximated by a power law in time $N_D \approx t^x$.

The results presented here differ from our previous results in [Hawick and Playne, 2008]. This is due to the fact that the size of the three-dimensional system analyzed had a field length of 16 as opposed to the system here with a field length of 240. The domains in the small system decayed to two domains very quickly and skewed the results whereas the larger system here takes longer to reach two domains.

$$C_{(x,y,z)} = \begin{cases} \text{rgba}(0.5 - \frac{\sigma_{x,y,z}}{2}, 0.5 - \frac{\sigma_{x,y,z}}{2}, 0.5 + \frac{\sigma_{x,y,z}}{2}, 0.5), & \text{if } \sigma_{x,y,z} > 0.0 \\ \text{rgba}(0.5 + \frac{\sigma_{x,y,z}}{2}, 0.5 + \frac{\sigma_{x,y,z}}{2}, 0.5 - \frac{\sigma_{x,y,z}}{2}, 0.05), & \text{if } \sigma_{x,y,z} \leq 0.0 \end{cases} \quad (27)$$

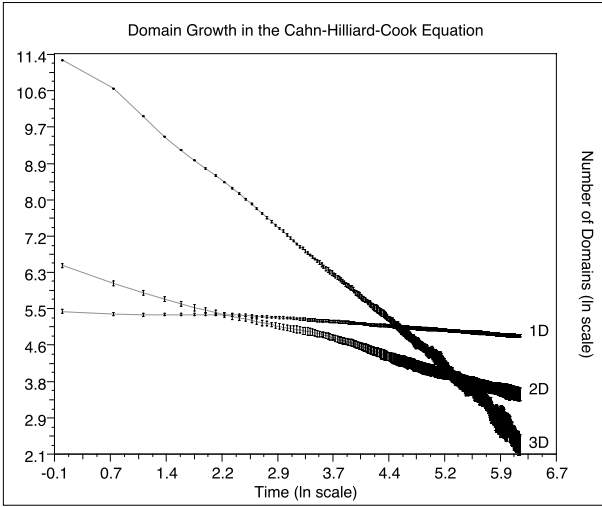


Figure 4: Domain growth plotted with time on a log-log scale, for systems of size 2048 cells; 256×256 cells; and $240 \times 240 \times 240$ cells respectively. Averages are over 30 separate configurations.

8 Simulating Field Equations

This paper has focused on simulating and visualizing the Cahn-Hilliard-Cook equation, but the same methods can be applied to almost any field equation model. Most field equation models update the cells within the field based on the values of the cells surrounding it. The pattern of the cells accessed is often referred to as a stencil. These stencils can work with a number of models in computational physics such as the Ising (bit variables), Potts (integer variables) or Heisenberg (floating point vector) spin models as well as in many cellular automaton and simple image processing algorithms

The key feature of stencil based applications is their use of relatively localised data on a regular mesh to update individual variables on the mesh. For example, the very simple Forward Time Centred Space solution of the Laplace Equation involves the discretisation of the field variable ψ on a mesh of some dimensionality - we use a 2d mesh here for illustration - and the iterative update of values $\psi_{i,j}$ according to:

$$\psi_{i,j} = \psi_{i+1,j} + \psi_{i-1,j} - 4\psi_{i,j} + \psi_{i,j+1} + \psi_{i,j-1} \quad (28)$$

This is illustrated in Figure: 5, showing a 5-point stencil op-

erator (the central point and its four nearest neighbours on a 2d square mesh) applied to a data field of integer values. The stencil operator in Figure: 5 corresponds to a central difference formulation of the ∇^2 operator.

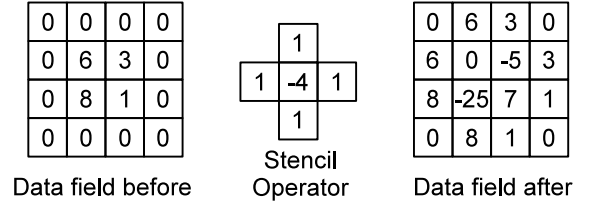


Figure 5: Application of 5-point stencil operator to 2d data field.

As we have discussed in Table: 1 these ideas generalize appropriately to our Cahn-Hilliard equation. More complex stencils can be constructed for various image processing operations. For example, edge detection or convolution. For 2 dimensional images, each stencil is a 2d image itself, with values that are not necessarily integer in value. It is convenient to adopt the convention that the stencils are constructed as centred with an odd length of edge, although stencils need not be square and may be rectangular. The idea generalises to higher dimensions and allows volume stencils to operate on voxel data on a regular mesh.

Application of stencil $S_{k,l}$ to an image $I_{i,j}$ might be expressed as:

$$I_{i,j} \mapsto \sum_{k,l} S_{k,l} \cdot I_{i,j} \quad (29)$$

for each pixel value (i,j) in image $I_{i,j}$.

While the stencil operation simply produces a linear summation of each pixel value and its neighbouring values, weighted by the corresponding stencil elements, some additional specification is necessary to define this operation at the boundary pixel values. For the purposes of manipulating images, it is convenient to assume all terms corresponding to pixel values outside the image are set to zero. This is not necessarily the case for a stencil operation used to solve a partial differential equation where the data field may be chosen to have cyclic boundaries or some value other than zero.

These operations are often not computationally very intensive, especially for relatively small stencils. The computational cost of looping over pixel values may be comparable

to the cost of doing the arithmetic on modern computational systems. It is possible to construct stencil operations that are not linear however, and where each stencil element is a functional rather than a simple weight.

Applying these stencil techniques to large fields, images or other data sets can be computationally challenging. It is therefore interesting to consider how these operations can be decomposed onto a parallel architecture. For many field equations, the order in which the cells are updated is not important, provided that the time-steps of the simulation remain synchronized. This allows the simulations to be easily split up into many tasks which can be distributed to the processors of the parallel architecture.

One parallel architecture that is particularly suited to performing these stencil operations is that of a Graphics Processing Unit (GPU) [A. Leist et al., 2008]. With the release of a number of GPGPU (General-Purpose computation on GPUs) APIs in recent years, it has become increasingly easy and popular to utilize GPUs for simulations. GPUs are especially suited to simulating field equations as they have optimizations designed specifically for image processing. As the stencil operations of a field equation simulation and those of an image processing task are almost identical in nature, GPUs are well-suited to processing any stencil-based field equation simulation.

9 Conclusions

We have presented results from some numerical experiments on the Cahn-Hilliard-Cook equation and discussed the relative merits of different integration algorithms. While it is possible to use an adaptive step size method for time integration we find the fixed step size fourth-order Runge-Kutta algorithm entirely adequate and indeed more useful for studying regular time spaced samples.

Graphics libraries such as JOGL provide a manageable interface to an interactive simulation system and we have been able to study interactively the early stages of the three dimensional system for relatively interesting mesh resolutions.

Other equations such as the Time-dependent Ginzburg Landau equation employ a complex field variable and we are presently experimenting with graphical techniques to display such a field using partially opaque coloured values and rendered arrows to show phase.

Generally all these stencil-like applications are amenable to the techniques we have presented, and we are optimistic about the potential of technologies such as GPUs for future optimisations.

References

- [A. Leist et al., 2008] A. Leist, D., Playne, and Hawick, K. (2008). Exploiting graphical processing units for data parallel scientific applications. Technical Report CSTN-065, Massey University.
- [Allen and Tildesley, 1987] Allen, M. and Tildesley, D. (1987). *Computer simulation of liquids*. Clarendon Press.
- [Binder, 1988] Binder, K. (1988). Theory of First Order Phase Transitions. Mainz Preprint.
- [Binder, 1989] Binder, K. (1989). Mechanisms for the decay of unstable and metastable phases: Spinodal decomposition, nucleation and late-stage coarsening. In Stocks, G. M. and Gonis, A., editors, *Alloy Phase Stability*, pages 233–262. Kluwer Academic.
- [Bryson and Russell, 2007] Bryson, T. and Russell, K. (2007). Java Binding for OpenGL (JOGL).
- [Buzbee et al., 1970] Buzbee, B., Golub, G., and Nielson, C. (1970). On Direct methods for solving Poisson’s equation. *SIAM J.Num.Analysis*, 7:627–656.
- [Cahn and Hilliard, 1959] Cahn, J. and Hilliard, J. (1959). Free energy of a non-uniform system III. Nucleation in a two point compressible fluid. *J.Chem.Phys.*, 31:688–699.
- [Cook, 1970] Cook, H. (1970). Brownian Motion in Spinodal De-composition. *Acta.Met*, 18:297–306.
- [Hawick, 1991] Hawick, K. A. (1991). Domain Growth in Alloys. Edinburgh University, Ph.D. Thesis.
- [Hawick and Playne, 2008] Hawick, K. A. and Playne, D. P. (2008). Modelling and visualizing the Cahn-Hilliard-Cook equation. In *Proceedings of 2008 International Conference on Modeling, Simulation and Visualization Methods (MSV’08)*, Las Vegas, Nevada.
- [Milchev et al., 1988] Milchev, A., Heermann, D. W., and Binder, K. (1988). Monte-carlo simulation of the Cahn-Hilliard model of spinodal decomposition. *Acta. Metall.*, 36(2):377–383.
- [Press et al., 1988] Press, W., Flannery, B., Teukolsky, S., and Vetterling, W. (1988). *Numerical Recipes in C*, chapter 17, pages 636–688. Cambridge University Press. Partial Differential Equations.
- [Toral et al., 1988] Toral, R., Chakrabarti, A., and Gunton, J. D. (1988). Numerical study of the Cahn-Hilliard equation in three dimensions. *Phys. Rev. Lett.*, 60(22):2311–2314.
- [Tuszynski et al., 1990] Tuszynski, J., Skierski, M., and Grundland, A. (1990). Short-range induced critical phenomena in the Landau-Ginzburg model. *Can.J.Phys.*, 68:751–755.